Journal of Hazardous Materials 338 (2017) 447–457

Contents lists available at ScienceDirect

Journal of Hazardous Materials

journal homepage: www.elsevier.com/locate/jhazmat

Magnetically separable sulfur-doped $SnFe_2O_4$/graphene nanohybrids for effective photocatalytic purification of wastewater under visible light

Yuefa Jia [a], Changjin Wu [a], B.W. Lee [a], Chunli Liu [a,*], Seokwon Kang [b], Taehyoung Lee [b], Yun Chang Park [c], Ran Yoo [d], Wooyoung Lee [d]

[a] Department of Physics and Oxide Research Center, Hankuk University of Foreign Studies, Yongin 17035, Republic of Korea
[b] Department of Environmental Science, Hankuk University of Foreign Studies, Yongin 17035, Republic of Korea
[c] Department of Measurement and Analysis, National Nanofab Center, Daejeon 34141, Republic of Korea
[d] Department of Materials Science and Engineering, Yonsei University, Seoul , 03722, Republic of Korea

HIGHLIGHTS

- Magnetically separable sulfur-doped $SnFe_2O_4$/graphene was prepared by hydrothermal method.
- The sulfur-doped $SnFe_2O_4$/graphene shows greatly improved photocatalytic degradation of aqueous chlorotetracycline.
- The sulfur-doped $SnFe_2O_4$/graphene has a larger rate constant than $SnFe_2O_4$ and $SnFe_2O_4$/graphene.
- Photocatalyst could be separated by an external magnetic field.
- The photocatalytic mechanism of sulfur-doped $SnFe_2O_4$/graphene was investigated.

GRAPHICAL ABSTRACT

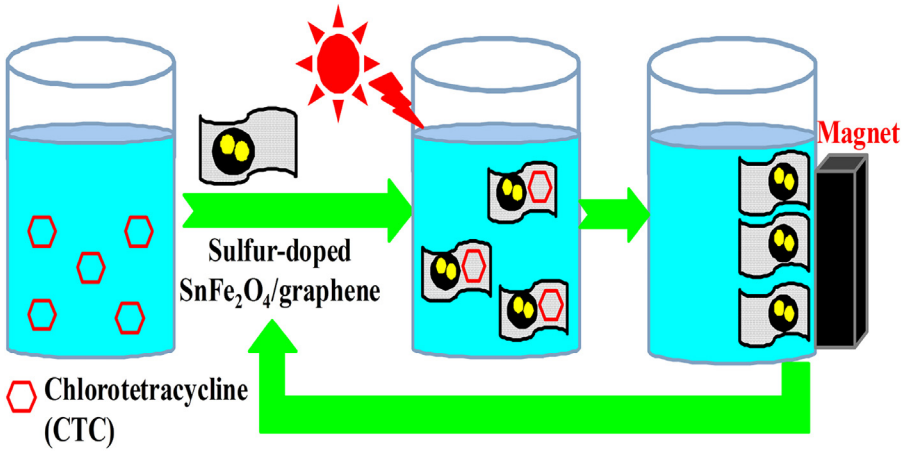

ARTICLE INFO

Article history:
Received 7 April 2017
Received in revised form 24 May 2017
Accepted 29 May 2017
Available online 1 June 2017

Keywords:
Sulfur
$SnFe_2O_4$
Graphene
Photocatalytic
Chlorotetracycline

ABSTRACT

In this report, magnetically recoverable sulfur-doped $SnFe_2O_4$/graphene (S-SFO/GR) nanohybrids have been successfully developed via a facile solvothermal method. The characterizations on the structural, morphology, and optical properties of the nanohybrids indicate that S-SFO particles are successfully embedded on the GR nanosheets. The photocatalytic activity has been evaluated by photocatalytic degradation of chlorotetracycline under visible light irradiation. Among the composites with various mass ratios, the quasi-first-order rate constant of the nanohybrids formed with 9 wt% S in SFO and 15 wt% GR (9S-SFO/GR-15) can reach as high as 1.83 min^{-1}, which is much higher than that of SFO (0.68 min^{-1}) and SFO/GR (0.91 min^{-1}), confirming the important role of S and GR for the photocatalytic process. The combination of the three components of S, SFO, and GR has enhanced the visible light absorption capability and inhibited the recombination of photogenerated electron-hole. The 9S-SFO/GR-15 nanohybrids can be recovered easily by a magnet and reused for five times with remained photocatalytic efficiency

* Corresponding author.
E-mail address: chunliliu@hufs.ac.kr (C. Liu).

http://dx.doi.org/10.1016/j.jhazmat.2017.05.057

about 70%. A possible catalytic mechanism explaining the efficient photocatalytic performances of the prepared nanohybrids has been proposed.

1. Introduction

Wastewater containing tetracyclines (TCs) pollutants has caused a great attention due to its negative impact on both ecosystem and human health [1]. Chlorotetracycline (CTC) belongs to the TCs antibiotic groups, and is one of the most widely detected TCs in wastewater and sediments [2]. Previous studies have reported that residual CTC in the wastewater system potentially endangers the population health and the balance of nature [3,4]. Accordingly, the complete removal of CTC from wastewater or natural water is an important environmental task. Generally, the wastewater treatment factories use the conventional methods such as biodegradation and absorption of the CTC on suitable materials, which suffer from either low efficiency or high cost [4]. As compared to the traditional purification methods, photocatalytic degradation of CTC has been considered as a more promising approach due to its advantages in energy-saving and thorough decomposition of the organic pollutants [5].

Oxide semiconductors are widely investigated materials for the photo- decomposition of organic and toxic pollutants in waste water [6]. Among them, TiO_2 has been the most popular choice as a photocatalyst for environmental remediation because of its outstanding stability, high photocatalytic activity, nontoxicity, and low cost [7]. However, the band gap energy (~3.2 eV) corresponding to UV light wavelength limits the application of TiO_2 because UV light occupies only around 5% of solar light as compared to visible light (52%) [8]. Furthermore, since the photocatalytic processes are usually implemented in heterogeneous systems, the re-collection of the suspended photocatalyst materials from the reaction medium after the photocatalytic process presents another challenge for the design of photocatalyst.

Recently spinel ferrite nanoparticles, such as $CoFe_2O_4$, $ZnFe_2O_4$, $NiFe_2O_4$, $SnFe_2O_4$, etc. have been widely studied as photocatalysts due to their visible light driven photoactivity and easy magnetic retrievability [9–12]. However, MFe_2O_4 (M = Zn, Co, Ni, Mn, etc.) alone showed unsatisfactory efficiency under visible light irradiation due to the fast recombination of photogenerated electron-hole pairs [13]. Two typical approaches have been adopted to overcome this problem, i.e., preparing composite materials with graphene (GR) or doping with impurities.

GR, which is a 2D material with many interesting physical and chemical properties, has been considered as a high performance support for photocatalysts. Nanocomposites supported on GR have been reported to have dramatically enhanced adsorption and significantly less recombination of photogenerated electron-hole pairs [14–17]. For example, it was reported that the binary composites of GR/MFe_2O_4 (M = Co, Zn, Ni, etc.) showed much enhanced photocatalytic activities compared to single phase MFe_2O_4 or GR [18–24]. Regarding the doping approach, transition metals (Ag or Pd) as dopants were utilized to increase the adsorption of visible light and also inhibit the recombination of the electron-hole pairs in MFe_2O_4 [9,11]. However, because the metal nanoparticles were mostly decorated on the surface of MFe_2O_4, metal-doped MFe_2O_4 can have drawbacks such as potential toxicity and metal leaching during repeated usages. Accordingly, the nonmetal-doped process is more desirable when efficiency and environmental –friendliness are considered [8]. Recent studies have reported that doping nonmetal element such as sulfur (S) in MFe_2O_4(M = Zn and Co) could not only have narrow band gaps but also possess high effective separation of electrons and holes, which exhibits remarkably enhanced photocatalytic activities compared to single phase MFe_2O_4 [25,26]. Based on the above mentioned results, it is reasonable to expect further improvement in the photocatalytic activity through modification of MFe_2O_4 with S and GR. The difficulty in preparing the ternary nanohybrids consisted of S/MFe_2O_4/GR lies in the effective doping of S in ferrite. In reported studies, S doped MFe_2O_4 (M = Zn and Co) was usually prepared by using solid-state reaction [25–27]. The high temperature calcination (typically at more than 500 °C) can cause the grain growth and the evaporation of S, which makes it hard to control the morphology and the S doping concentration [28–30]. Therefore, low temperature synthesis of S-doped ferrite nanoparticles is desired for synthesizing S doped ferrites and related nanocomposites.

In this work, we report the preparation of magnetically recoverable S-$SnFe_2O_4$(SFO)/GR nanohybrids and their enhanced photocatalytic properties via a facile low temperature solvothermal method. SFO was recognized only recently for its photocatalytic performance due to its narrow band gap (2.53 eV), non-toxic, natural abundance, excellent ferromagnetic properties for magnetic separation from suspensions, and overall environmental benignity [12,31,32]. We used thiourea (CH_4N_2S) as the S precursor and prepared S doped SFO nanoparticles with controlled S concentration through a hydrothermal process. The photocatalysis experiment demonstrated that S-SFO/GR nanohybrids show significantly enhanced photocatalytic degradation of CTC as compared with SFO and S-SFO under visible light irradiation. The recyclability revealed that the S-SFO/GR nanohybrids had acceptable photocatalytic stability. Possible mechanism for the transfer of photogenerated carriers was also further proposed.

2. Experiment section

2.1. Synthesis of S-SFO/GR nanohybrids

S-SFO nanoparticles were prepared with a solvothermal method. First, $SnCl_2$ (0.034 M), $FeCl_2{\cdot}4H_2O$ (0.068 M) and certain amount of CH_4N_2S were dissolved in 50 mL ethylene glycol under constant stirring to form a solution. A suitable amount of aqueous NaOH and NH_4OH was added to the above solution and pH of the solution was maintained at >10. Subsequently, the mixture was put into a 100 mL Teflon vessel and then sealed in an autoclave and heated at 200°C for 15 h. Finally, the resulting products were washed using ethanol for several times and dried in air at 80°C for 12 h. A series of S-SFO were prepared by changing the theoretical mass percentage of S to SFO (0, 5, 9, 15, 30 wt%), which are denoted as SFO, 5S-SFO, 9S-SFO, 15S-SFO and 30S-SFO, respectively.

S-SFO/GR nanohybrids were prepared with the same method to the S-SFO. The whole preparation process is out-lined in Scheme 1. Briefly, $SnCl_2$, $FeCl_2{\cdot}4H_2O$ and certain amount of CH_4N_2S were dissolved in 60 mL ethylene glycol under constant stirring. A suitable amount of aqueous NaOH and NH_4OH was added to the above solution and pH of the solution was maintained at >10. Subsequently, the mixture was put into a 100 mL Teflon vessel and then sealed in an autoclave and heated at 200 °C for 15 h. The reacted solution containing S-SFO was cooled naturally to room temperature. Then 75 mg of graphene oxide (GO, Sigma-Aldrich Chemicals Co.) was

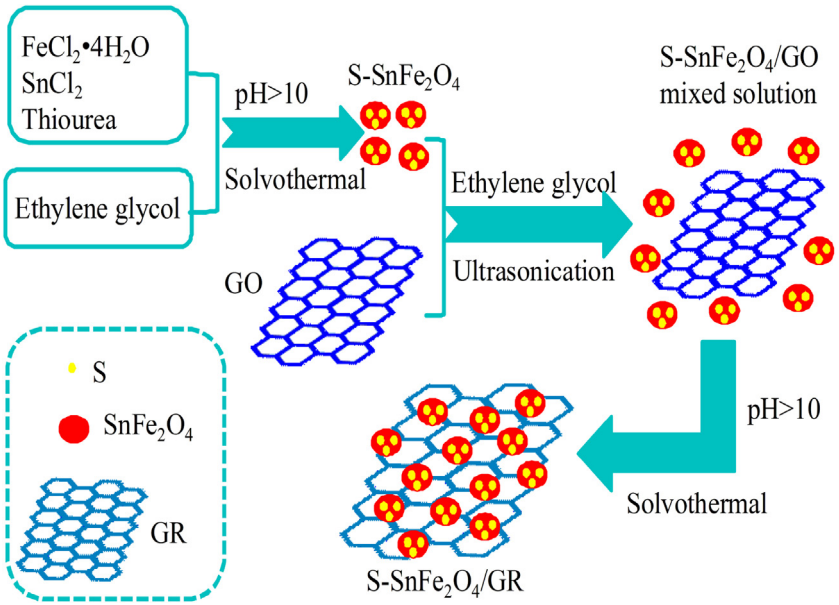

Scheme 1. The preparation route of the S-SFO/GR nanohybrids.

added into the autoclave containing the S-SFO solution with sonication for 1 h. The pH value of the solution was adjusted to 10 by adding 5 M NaOH. After stirring for 1 h at room temperature, the autoclave with the mixture solution was heated at 180 °C for 12 h. After the reaction, the S-SFO/GR nanohybrids product was separated from the solution with a magnet and rinsed with water and ethanol twice, and dried in vacuum at 80 °C for 24 h.

As described in Scheme 1, GO dispersed in ethylene glycol was first exfoliated during the sonication process, and then reduced to GR in the following solvothermal step. Ethylene glycol was used as both reducing agent and solvent. NaOH alters the alkalinity and assists the reduction of GO. The carboxyl and hydroxyl groups decorated on the basal plane and sheet edges of GO [33], which can act as potential anchor sites for S-SFO nanoparticles. The formation of SFO nanoparticles in S-SFO/GR nanohybrids can be represented as following equations [34]:

$$Fe^{2+}+2OH^{-} \rightarrow Fe(OH)_2 \quad (2)$$

$$Fe(OH)_2+OH^{-} \rightarrow \beta - FeOOH+H_2O \quad (3)$$

$$Sn^{2+}+2OH^{-} \rightarrow Sn(OH)_2 \quad (4)$$

$$Sn(OH)_2+\beta - FeOOH \rightarrow SnFe_2O_4 + H_2O(Solvothermal) \quad (5)$$

Therefore S-SFO/GR nanohybrids can be synthesized using the solvothermal process. The products with 75 mg of GO (15 wt%) was described as SFO/GR-15, 5S-SFO/GR-15, 9S-SFO/GR-15, 15S-SFO/GR-15, and 30S-SFO/GR-15 were obtained with SFO, 5S-SFO, 9S-SFO, 15S-SFO, and 30S-SFO, respectively. To determine the effects of the GR loading, the 9S-SFO/GR nanohybrids with different amounts of GO (25, 125, and 200 mg) were prepared using the same preparation method, and the corresponding products were denoted as 9S-SFO/GR-5, 9S-SFO/GR-25, and 9S-SFO/GR-40, respectively.

2.2. Characterization methods

The phase structure of the samples were identified by a Rigaku MiniFlex 600 X-ray diffraction (XRD) using Cu K_α (λ = 0.15418 nm) radiation. Lakeshore 7403 vibrating sample magnetometer (VSM) was used to measure the magnetic properties of samples. Nitrogen adsorption isotherms and Brunauer, Emmett, and Teller (BET) surface area were measured by a Micromeritcs ASAP 2020 analyzer. The samples were characterized by a LabRAM ARAMIS Raman spectrometer (LabRAM HORIBA Jobin Yvon, Edison, NJ) with excitation source of an Ar laser (λ = 514.532 nm, 0.5 mW). Fourier transfer infrared spectroscopy (FT-IR) was recorded using a Nicolet Avatar 370 FT-IR. The UV–vis diffuse reflectance spectra (UV–vis DRS) were performed on a U3010 UV–vis spectrometer. The morphology and microstructure of the samples were observed by a field emission scanning electron microscopy (FESEM, Hitachi-S4800) equipped with energy-dispersive X-ray (EDX) and a field emission transmission electron microscope (FETEM, JEOL, JEM-ARM200F). The X-ray photoelectron spectroscopy (XPS) measurements were performed using a mono-chromated Al K_α X-ray source ($h\nu$ = 14 86.6 eV) at 15 kV/150 W. The spot size used was 400 mm (Theta Probe AR-XPS System, Thermo Fisher Scientific, Waltham, MA, USA). A Sievers Model 800 TOC Analyzer coupled with Inorganic Carbon Removal (ICR) module was used for measuring total organic carbon (TOC) in the sample.

2.3. Photocatalytic degradation measurement

The photocatalytic experiments are carried out in the device as described elsewhere [31,32]. The experimental procedure was as follows: 70 mg of photocatalyst was first suspended in 70 mL CTC at pH = 7.48 (50 mg/L in H_2O, $C_{22}H_{23}ClN_2O_8 \cdot HCl$: ≥75%, Sigma-Aldrich Chemicals Co.) in a quartz tube, which was then sonicated for 10 min and stirred at 900 rpm continuously for 1 h before light irradiation to ensure that the photocatalyst surface was saturated with CTC molecules. Next, the mixture was then irradiated with a 300 W iodine tungsten lamp located 25 cm away from the visible source. All the tests were performed at room temperature(25 ± 1 °C). At given time intervals of irradiation, 5 mL of the suspension were withdrawn and magnetically separated to remove essentially all the catalyst. The supernatant was centrifuged and then filtered through a syringe filter [polyethersulfone (PES) membrane, pore size 0.2 μm, filter diam. 13 mm (Sigma)] to remove trace of residual catalyst. The residual concentration of CTC was monitored using a UV–vis spectrophotometer (Cary 5000 UV–vis-NIR, Agilent) at 365 nm.

The degradation rate (DR) was estimated according to the following formula (Eq. (1)) [35,36]:

$$DR(\%) = (A_0 - A_t)/A_0 \times 100\% = (C_0 - C_t)/C_0 \times 100\% \quad (1)$$

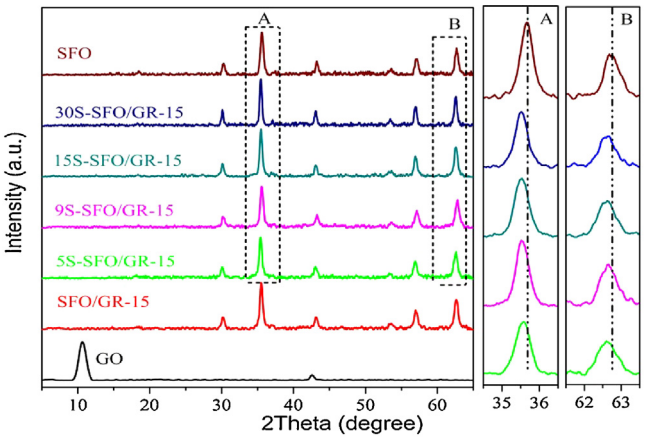

Fig. 1. XRD patterns of all samples.

where A_t is the absorbance of CTC solution after the irradiation time, A_0 is the initial absorbance of CTC solution before degradation, C_t is the solution concentration of CTC, and C_0 is the initial concentration of CTC solution.

The photocatalytic stability of S-SFO/GR nanohybrids was investigated by recycling tests. After each cycle of photodegradation test, S-SFO/GR photocatalyst was separated from CTC solution using a lab magnet and washed with deionized water and ethanol, dried at 120 °C for 4 h and put into the same volume of fresh CTC solution for the next reaction cycle. The process was repeated for five times.

3. Results and discussion

3.1. Characterization of S-SFO/GR nanohybrids

Fig. 1 shows the XRD diffraction patterns of all samples. The magnified patterns of two principal peaks (A and B) are also inserted at the right part of Fig. 1. The diffraction peaks of GO shows a strong peak at 2θ values of 10.62°, originated from its (001) reflection. Another peak around $2\theta = 42.58°$ can also be observed, which is the characteristic (100) peak of residual unoxidized graphite [24]. It is obvious that the SFO and S-SFO/GR-15 nanohybrids are exhibited similar XRD patterns. The diffraction patterns of those samples are matched well with the Fe_3O_4 (JCPDS card No.11-0614) and those published works in the literature for SFO [12,31,32], and no peak shift was observed when GO was introduced into the S-SFO, meaning that the formation of the nanohybrids with the present weight ratios of GO has a negligible effect on the crystal phase of S-SFO. The disappearance of the graphite (100) and GO (001) diffraction peaks in the nanohybrids is due to the small amount of GO (15 wt%) used and the broken regular stack of GO due to the crystal growth of S-SFO nanoparticles between the interlayers during the solvothermal treatment [21,23]. Meanwhile, the narrow peaks of the XRD patterns evidence the high crystallinity and no impurities peaks are detected. A detailed inspection on the magnified principal peaks (shown at the right side of Fig. 1) reveals that the principal peaks shift slightly to lower angle (especially for peak A and Peak B) with the increase of doping amount of S, which can be attributed to the lattice expansion. Because the ionic radius of S (1.7 Å) is larger than that of O (1.22 Å) [37], the SFO lattice expanded when it incorporated increasing amounts of S. It implies that S was effectively incorporated into the SFO. The main XRD peaks of 9S-SFO/GR-5, 9S-SFO/GR-25 and 9S-SFO/GR-40 are similar to 9S-SFO/GR-15 nanohybrids, and the diffraction peak at 24.98° is strengthened with increasing the mass fraction of GO, which can be assigned to the (002) plane of GR (Fig. S1).

Fig. 2a shows a comparison of the Raman spectra of GO, SFO, 9S-SFO, SFO/GR-15 and 9S-SFO/GR-15. In the case of GO, the two peaks observed at 1348 and 1599 cm^{-1} correspond to the well-documented D band and G band, respectively. The intensity of D band is stronger than that of G band, implying the presence of high density of defects and structure disorder in GO. In comparison with GO, significant shifts were observed in the Raman peaks of SFO/GR-15 and 9S-SFO/GR-15 nanohybrids. The D and G bands were shifted from 1348 and 1599 cm^{-1} for GO to 1335 and 1585 cm^{-1} for SFO/GR-15, 1335 and 1580 cm^{-1} for 9S-SFO/GR-15, respectively. These significant vibrational band shifts suggested the existence of charge transport between GR and SFO or 9S-SFO. For the SFO/GR-15 and 9S-SFO/GR-15 nanohybrids, the peaks below 1000 cm^{-1}(325, 482 and 672 cm^{-1}) corresponding to the vibrations of SFO [33], which indicates the combination of SFO or 9S-SFO with the GR, which was also supported by the XRD analysis results. In addition, the D/G intensity ratio for SFO/GR-15 (1.41) and 9S-SFO/GR-15 (1.78) shows an enhanced value as compared with that of pure GO (1.05). This change suggests a decrease in the average size of the sp^2 hybridized GR domains during the solvothermal process [19].

Nitrogen adsorption-desorption isotherm measurements were performed to characterize the specific surface areas of 9S-SFO and 9S-SFO/GR-15 (Fig. 2b). Both samples exhibited type IV isotherm curves, indicating the presence of mesoporous structures (2–50 nm) [24,38]. BET specific surface area of 9S-SFO/GR-15 was about 95.361 m^2/g, which was much larger than that of 9S-SFO (21.534 m^2/g). The increased specific surface area of the nanohybrids can be attributed to the introduction of GR sheets as expected. Therefore, the high surface area of nanohybrids provides sufficient adsorption and active sites to facilitate the diffusion of pollutant and reaction products into/out the photocatalyst, which consequently leads to an enhanced photocatalytic activity.

The magnetic behavior of the as-synthesized samples was investigated using a VSM at room temperature. As shown in Fig. 2c, the saturation magnetization (M_s) of SFO, 9S-SFO, SFO/GR-15 and 9S-SFO/GR-15 were 47, 66, 38 and 55 emu/g, respectively. The M_s values of SFO/GR-15 and 9S-SFO/GR-15 were lower than those of pure 9S-SFO and SFO due to the presence of GR nanosheets in nanohybrids. It is also noted that the M_s values of nanohybrids with S dopant were higher than those of the non-doped counterpart. This observation can be attributed to the following reasons. Firstly, Fe ions were migrated from the tetrahedral-site to the octahedral-site with S doping during the solvothermal process, which may have caused the increase of M_s [27]. Additionally, the increase in the M_s values is in accordance with the increased particle size of S-SFO after doped with S due to less magnetically dead layer on the surface of the particles [39]. The inset of Fig. 2c evidenced that the 9S-SFO/GR-15 nanohybrids could be easily separated from the solution after the photocatalytic reaction using a magnet.

Fig. 2d–f shows the FESEM images of the GO, 9S-SFO, and 9S-SFO/GR-15 samples. As shown in Fig. 2d, GO is consisted of big sheets with ripples and paper-like structure with thin layers, which can certainly provide sufficient surface area to load the 9S-SFO particles. The aggregated 9S-SFO particles are shown in Fig. 2e with various cluster size. Fig. 2f shows that the 9S-SFO particles (with sizes ranging from ~20 to 30 nm) are successfully attached on the GR nanosheets. It is worth noting that the size of 9S-SFO/GR-15 is comparable with the size of 9S-SFO, suggesting that the 9S-SFO crystal growth is effectively inhibited by the ultrathin GR nanosheets during the thermal treatment [19]. The EDX measurement of 9S-SFO/GR-15 nanohybrids further confirms the co-existence of C, O, Fe, Sn, and S elements (Fig. 2g). The signal of Pt is from the pretreatment.

The morphology and element analysis of 9S-SFO/GR-15 nanohybrids were further depicted by FETEM in Fig. 3. These images also

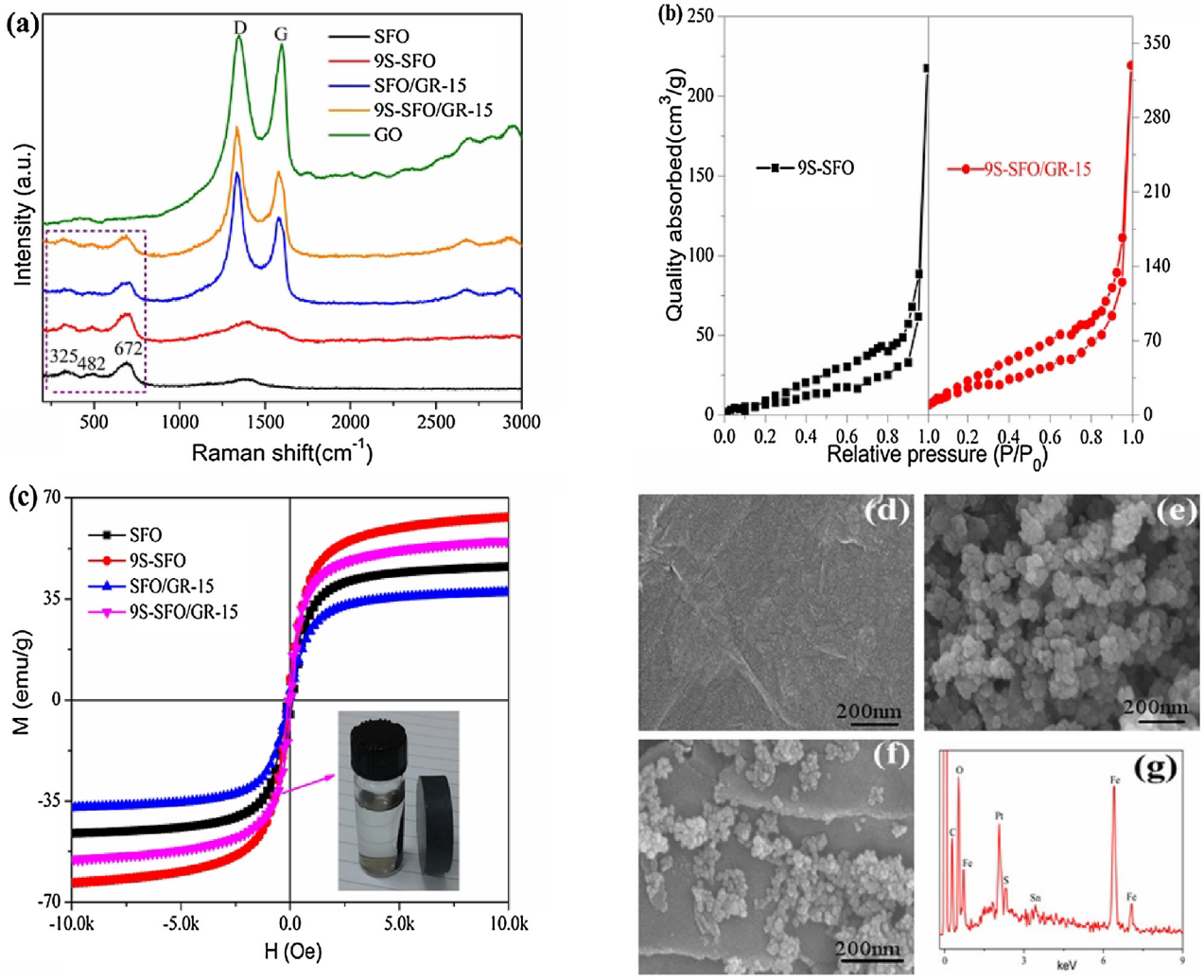

Fig. 2. (a) Raman spectra; (b) N_2 adsorption-desorption isotherm; (c) Magnetization curves at 296 K, inset shows the magnetic separation process of 9S-SFO/GR-15; (d–f) FESEM of GO, 9S-SFO, and 9S-SFO/GR-15; (g) the EDX analysis of 9S-SFO/GR-15.

clearly suggest that the 9S-SFO nanoparticles with size of about 25 nm are randomly dispersed on the surface of GR nanosheets (Fig. 3a and b), in good consistency with the observation from FESEM. It can be also seen that GR nanosheets were single layers with large surface area, which can provide more active adsorption sites and enhance charge separation for photocatalyst. Furthermore, the EDS-mapping analysis results of C and Fe elements (Fig. 3c and d) in the red framed region of Fig. 3a clearly reveal that the presence of C from the GR sheet and the shape of 9S-SFO nanoparticles in nanohybrids. More importantly, the FETEM image of 9S-SFO/GR-15 nanohybrids shows that 9S-SFO particles have cube-shaped morphology (Fig. 3e). The lattice fringes can be clearly seen in the FETEM images, which corresponds to the inter plane distance of 4.89 Å for the SFO (111) planes (inset of Fig. 3e). The Fig. 3f displays the fast Fourier transform (FFT) of red framed region of Fig. 3e, which shows four different types of spots that may be indexed to the (220), (400), (040), and (440) planes of well-crystallized $SnFe_2O_4$ in 9S-SFO/GR-15 nanohybrids, in good agreement with the XRD and Raman spectra observations.

XPS spectra were measured to investigate the chemical status of each element in the nanohybrids. The C1s XPS spectrum of GO is shown in Fig. 4a, which can de-convoluted into four distinct peaks at 284.4 eV for C—C/C=C/C—H, 285 eV for C—OH, 286.5 eV for C—O—C/C=O, and 287.7 eV for COOR, respectively [15,21]. The wide scan XPS spectrum of 9S-SFO/GR-15 nanohybrids were collected in Fig. 4b, which demonstrated clearly the existence of S, C, O, Fe, and Sn elements in the sample. As compared to Fig. 4a, the high resolution XPS spectrum of C1s peaks in 9S-SFO/GR-15 shows quite low intensity peaks of C—O—C/C=O (285.9 eV) and COOR (288.4 eV), indicating that the solvothermal treatment are effective in the reduction of GO to GR [21,22]. According to an earlier report by Liu et al. [40], the enhanced conductivity induced by the reduction of GO leads to more effective charge separation and low recombination rate during photocatalytic process, thus improved photocatalytic efficiency can be expected in the 9S-SFO/GR-15 nanohybrids system. Similarly, a detailed scan of S2p spectrum (Fig. 4d) can be fitted into four peaks. The two peaks at 163.18 eV and 164.23 eV can be attributed to $2p_{3/2}$ and $2p_{1/2}$ of the lower valence state of S^{2-} [41]. The binding energy at 167.74 eV and 168.91 eV are from S^{6+} $2p_{1/2}$ and S^{6+} $2p_{3/2}$, respectively, suggesting that S is in the highest oxidation state (+6) [42]. The ratio between S^{2-} and S^{6+} on the surface of the 9S-SFO/GR-15 is about 0.86. Hence, the valence states of the S element might also include S^{2-} and S^{6+} in the S-SFO lattice. Together with the EDX and EDS results, the XPS data further confirmed the doping of the element S into the SFO nanoparticles. The peaks of $Sn3d_{5/2}$ at 486.28 eV and $Sn3d_{3/2}$ at 494.78 eV can be assigned to Sn(IV) oxidation state (Fig. S2a) [31,43]. For the Fe2p spectrum (Fig. S2b), the peak of Fe

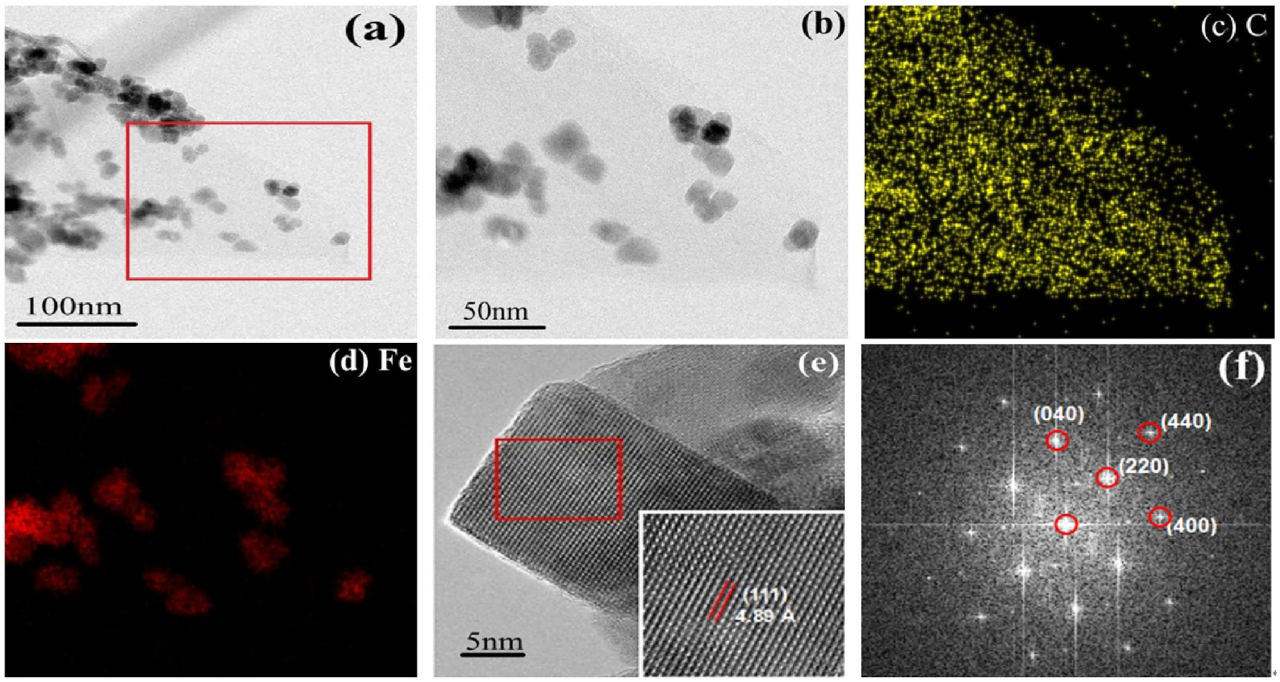

Fig. 3. (a) FETEM image of 9S-SFO/GR-15; (b) FETEM image of 9S-SFO/GR-15 in the red frame of (a); and EDS-mapping of C (c) and Fe (d); (e) the lattices (111) and (f) FFT pattern of 9S-SFO/GR-15. (For interpretation of the references to colour in this figure legend, the reader is referred to the web version of this article.)

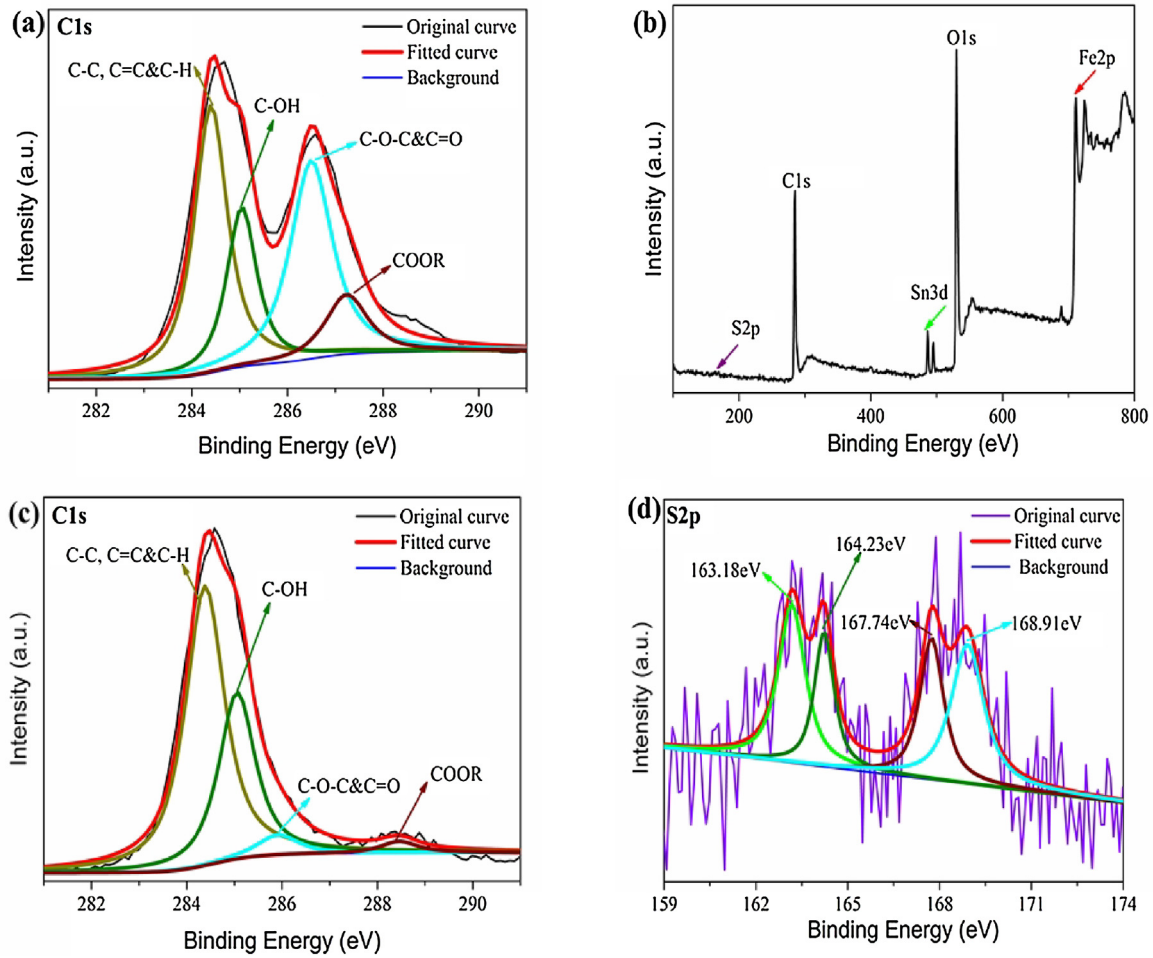

Fig. 4. (a) High-resolution XPS spectra of C1s peaks of GO; (b) wide scan XPS spectra of 9S-SFO/GR-15; (c) high-resolution XPS spectra of C1s peaks and (d) S2p peaks in 9S-SFO/GR-15.

$2p_{3/2}$ at 709.78 eV can be ascribed to the existence of Fe^{2+} oxide, and the other three peaks of Fe $2p_{3/2}$ located at 710.88, 712.48 and 715.08 eV was attributed to Fe^{3+} oxide [10,23]. The peak at 724.28 eV is attributed to Fe $2p_{1/2}$, and two shake-up satellite signals (718.58 and 732.48 eV) also suggest that Fe^{3+} in SFO [44]. The O1 s spectrum (Fig. S2c) can be deconvoluted into three different peaks at 529.68, 530.58, and 531.78 eV. The O1s binding energy of 529.68 eV was lattice oxygen binding with Fe and Sn (Fe-O and Sn-O), while the peaks located at 530.58 eV and 531.78 eV were attributed to the surface-absorbed oxygen species ($O_2^-{}_{ads}$ and $O^-{}_{ads}$) [45,46]. The $O_2^-{}_{ads}$ and $O^-{}_{ads}$ on 9S-SFO/GR-15 nanohybrids surface is the active oxygen, which plays an important role in the oxidation reaction [47].

All the above analyses accounted for the successful preparation of S-SFO/GR-15 nanohybrids.

3.2. Evaluation of photocatalytic activity

Fig. 5a and b shows the photocatalyst dependence of the absorbance evolution of CTC solution under visible light irradiation. The chemical structure of CTC was shown in the inset of Fig. 5a. As shown in Fig. 5a, no obvious change was observed in the peak intensity at 365 nm originated from the naphthacene ring structure of a CTC chain [4], indicating that CTC was barely destroyed with the presence of SFO as the time prolonged. On the other hand, the dramatic and continuous decrease in the absorption peak at 364 nm in Fig. 5b indicates the complete cleavage of the CTC molecules with the presence of 9S-SFO/GR-15 after 4 h.

Fig. 5c depicts the time evolution of the degradation efficiencies of various photocatalysts. With pure SFO, only 10% CTC solution was removed after 4 h irradiation, which is mainly due to the rapid recombination of photogenerated carriers in SFO. However, the degradation efficiencies increased with increasing S doping concentration up to 9% S-SFO, then decreased with further increasing S content. S doping has been reported to be effective in narrowing the band gap and forming defects, resulting in lower recombination rate of photogenerated e^--h^+ pairs [48]. But excessive doping may also suppress the active sites on the S-SFO surface because defects can play as the recombination centers for photogenerated e^--h^+ [49], which explains the decreasing in the photocatalytic activity of the nanohybrids with higher S concentration. Furthermore, as compared to S-SFO, all the S-SFO/GR-15 nanohybrids display a significantly enhanced degradation efficiency of CTC, implying that the synergistic effect between S-SFO and GR nanosheets led to the efficient separation of photogenerated carriers in the nanohybrid photocatalyst. Furthermore, the larger specific surface area in S-SFO/GR-15 photocatalyst could offer more surface active sites and photocatalytic reaction centers [21], resulting in the improved photocatalytic activity. Among all S-SFO/GR-15 samples, the 9S-SFO/GR-15 nanohybrids demonstrate the highest degradation efficiency. After adsorption and visible light illumination, the removal efficiencies of CTC solution were about 82% after 4 h.

Fig. 5d shows the photocatalytic activity of 9S-SFO/GR nanohybrids containing various mass percentage of GR ranging from 0% to 40%. Pure GO does not exhibit any capacity for the CTC degradation under visible light irradiation even though it possesses strong adsorption capability for CTC owing to high specific surface areas. For 9S-SFO/GR nanohybrids, degradation rate increased as the mass percentage of GR increased in the hybrid catalysts and reached a maximum value of 82% with 15% GR. The degradation rate then began to decrease with continued increases in GR contents (25% and 40%). Although increase in the GR content can improve the adsorption of CTC and the synergistic effect between GR and 9S-SFO, overload GR could shield the active sites on the 9S-SFO surface and decreasing the visible light absorption on the catalyst surface [50]. Based on this result, the 9S-SFO/GR-15 nanohybrid was used as a reference in the following experiments.

Fig. 5e shows the kinetic studies of the degradation of CTC with different photocatalysts. It was observed that the degradation of CTC over GO, SFO, SFO/GR-15, and 9S-SFO/GR-15 belong to the quasi-first-order kinetics as expressed with following equation [13,51]:

$$ln\frac{C_0}{C_t} = kt \tag{6}$$

where k is the quasi-first-order rate constant, C_0 is the equilibrium concentration of CTC, and C_t is the concentration at time t. The k value for CTC removal using GO, SFO, SFO/GR-15, and 9S-SFO/GR-15 are 0.25, 0.68, 0.91, and 1.83 min^{-1}, respectively, showing that the introduction of S and GR indeed enhances the photocatalytic performance of SFO.

Several ions and organics such as NO_3^-, C_2H_5OH, SO_4^{2-}, Ca^{2+}, bean oil, SiO_3^{2-}, and $NH_3{\cdot}H_2O$ are usually presented in wastewater, especially in the practical effluents from the textile and dyestuff industries. Results in Fig. 5f indicate that the degradation efficiency of CTC was enhanced in the presence of NO_3^-, which is due to the reactive species generated in nitrate solution [52]. C_2H_5OH ions exhibited minimal or negligible impacts. However, the SO_4^{2-}, Ca^{2+} ions, and bean oil would obviously affect the degradation of CTC. The SO_4^{2-} ions adsorbed on the 9S-SFO/GR-15 surface may de-activate GR/e^- and further suppress the reaction between e^- and O_2 to generate superoxide ($^{\bullet}O_2^-$) radicals [53]. The suppressed decomposition of CTC in the presence of Ca^{2+} may be related to competitive adsorption relationship between 9S-SFO/GR and Ca^{2+} [54]. GR demonstrated a fast adsorption performance toward various oil [55]. Thus, some oil molecules adsorbed on the 9S-SFO/GR-15 surface can reduce the possibility of capturing CTC and delocalized e^-. Meanwhile, the bean oil on the surface of CTC solution would reduce the dissolved oxygen content in the reaction solution, which had an effect on $^{\bullet}O_2^-$ radicals evolution rate over 9S-SFO/GR-15. The photocatalytic efficiency sharply decreased with the presence of SiO_3^{2-} due to 9S-SFO/h^+ sites were poisoned by SiO_3^{2-} [53]. $NH_3{\cdot}H_2O$, NH_4^+ would react with $^{\bullet}OH$ radicals or h^+ to form $(NH_2)_x$ radicals species and OH^- strengthens electric repulsion between CTC molecules and catalysts, which results in a significant loss of degradation efficiency for CTC [56]. Fig. 5f shows the following order in the CTC degradation efficiency when the above radicals are presented: NO_3^- > no ions and organics > C_2H_5OH > SO_4^{2-} > Ca^{2+} > bean oil > $NH_3{\cdot}H_2O$ > SiO_3^{2-}.

The wastewater from textile industries usually has a wide range of pH values. Therefore, the initial pH (2–11.2) of CTC solution was used with initial CTC concentrations of 50 mg/L and a constant photocatalyst dosage of 1 g/L. The removal efficiency of CTC at different initial pH values is displayed in Fig. S3a, the degradation efficiency of CTC reaches the maximum at pH = 7.48. This value is within the normal pH value range of practical wastewater, therefore no other adjustment of the pH value is necessary.

The effect of catalysts dosage 0.25–1.5 g/L to photo-activity of 9S-SFO/GR-15 is shown in Fig. S3b. The 9S-SFO/GR-15 displays a maximum efficiency when the catalysts dosage was increased to 1 g/L. Higher dosage causes a remarkably decreased efficiency presumably due to the reduction of the active sites and suppression of the visible light absorption [47,57,58]. Fig. S3c shows that the photocatalytic performance decreases continuously with increasing initial CTC concentration from 25 to 150 mg/L, which can be understood from the adsorption competition between CTC and intermediate CTC degradation products on catalyst surface.

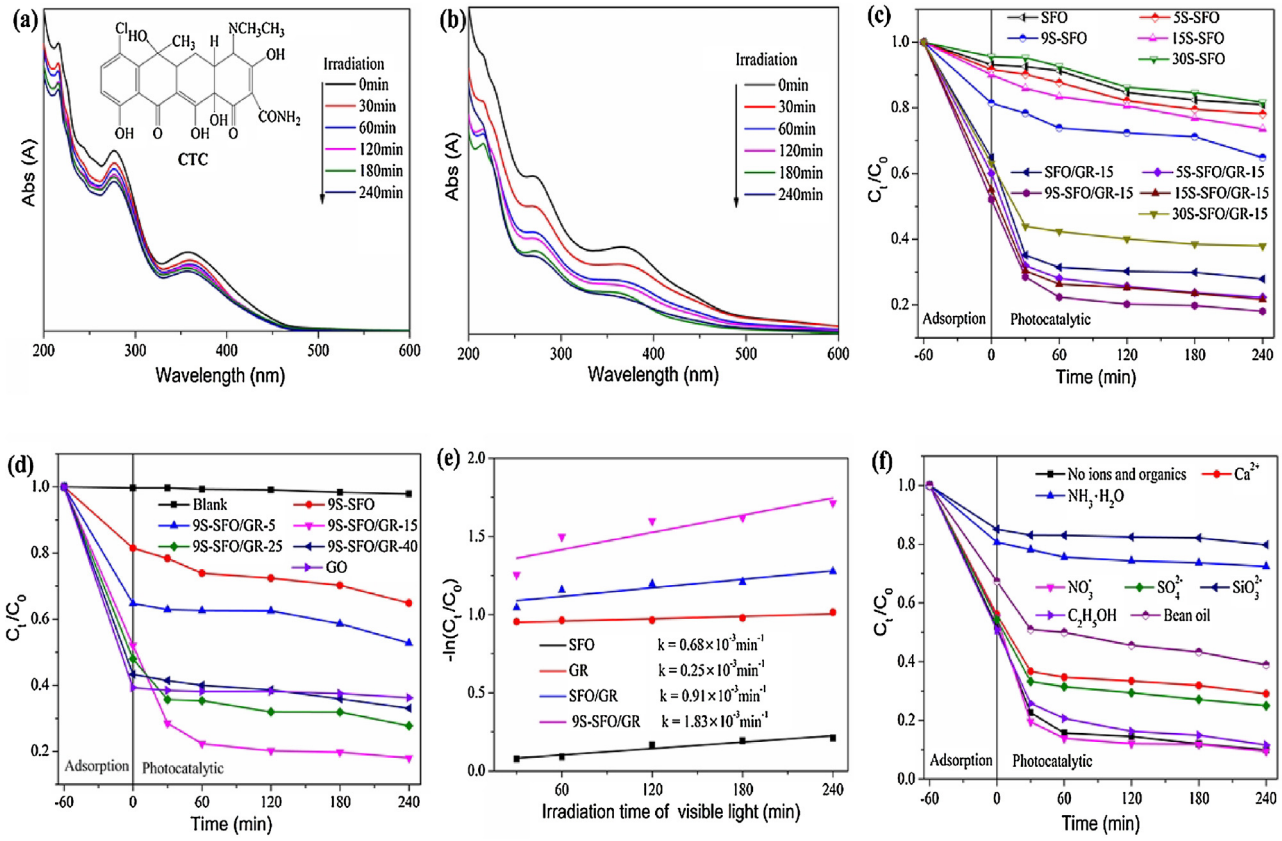

Fig. 5. Changes in UV–vis spectra of CTC with irradiation time in the presence of (a) SFO and (b) 9S-SFO/GR-15 (C_0 = 50 mg/L, [catalysts] = 1 g/L); inset Fig. 5a shows chemical structures of CTC. (c)photocatalytic degradation of CTC with different catalysts; (d) degradation of CTC over 9S-SFO/GR nanohybrids having various GR contents; (e) the kinetic curve of the degradation; (f) effect of ions and organics on the removal efficiency of CTC over 9S-SFO/GR-15 (C_0 = 50 mg/L, [catalysts] = 1 g/L, [Ca^{2+}, NO_3^-, SO_4^{2-} and SiO_3^{2-}] = 1 mmol/L, [$NH_3{\cdot}H_2O$, C_2H_5OH and bean oil] = 1:25/V:V).

3.3. Recyclability of the photocatalyst

Besides photocatalytic activity, stability and reusability are also two major challenges in employing photocatalytic materials in water remediation. The catalytic stabilities of 9S-SFO/GR-15 are tested through photocatalysis for five cycles using magnetically recollected photocatalyst (Fig. 6). Each run is carried out under the same conditions. Although the photocatalytic efficiency of the nanohybrids decreased gradually for the first three cycles, there was no further reduction from the third run. The initial lowering in the efficiency can be attributed to loss of the photocatalyst during recovery and the residual catalytic products on the surface of catalyst, which reduced the contact area between catalyst and pollutant [8]. After five cycles the photocatalytic efficiency of 9S-SFO/GR-15 for the degradation of CTC was maintained above 70%, respectively, indicating photocatalysts exhibited accepted photocatalytic stability in the CTC pollutants elimination.

To further confirm the stability of the 9S-SFO/GR-15 nanohybrids, the used catalyst after reaction was examined by XRD, FTIR, FESEM, and EDX, as shown in Fig. S4a–d. The XRD diffraction patterns of used 9S-SFO/GR-15 were no obvious changes before and after reaction (Fig. S4a). FTIR spectra of the SFO, SFO/GR-15, fresh and used 9S-SFO/GR-15 were similar and exhibited a characteristic absorption peak at 584 cm^{-1}, is attributed to Fe-O stretching vibration in SFO [12], and no obvious bands related to SO_3^{2-} or SO_4^{2-} groups are observed (Fig. S4b). Besides, the 9S-SFO with an average size of approximate 30–50 nm were still well anchored on silk-like GR nanosheets after reaction (Fig. S4c), which further confirm the high stability of 9S-SFO/GR-15. The EDX spectrum of used

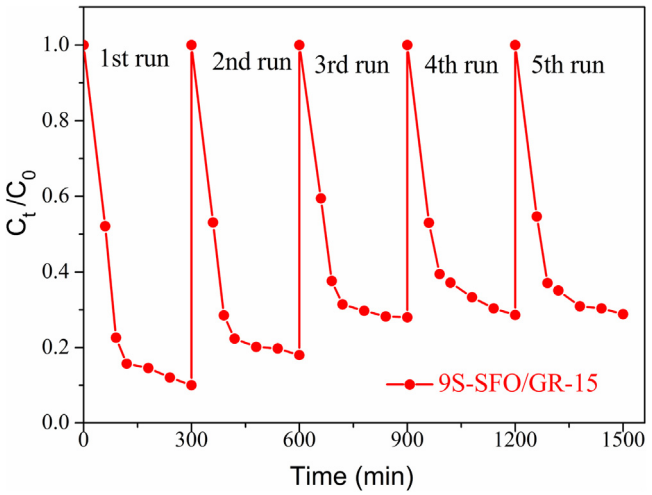

Fig. 6. Five recycle runs of 9S-SFO/GR-15 for CTC degradation (C_0 = 50 mg/L, pH = 7.4, [9S-SFO/GR-15] = 1 g/L).

9S-SFO/GR-15 reveal that the elements C, O, Fe, S, and Sn present in used sample (Fig. S4d), indicating the S in the crystal lattice of nanohybrids could be not eliminated by repetitious washing process.

All these results clearly reveal that the catalyst is very stable and can have a good catalytic activity.

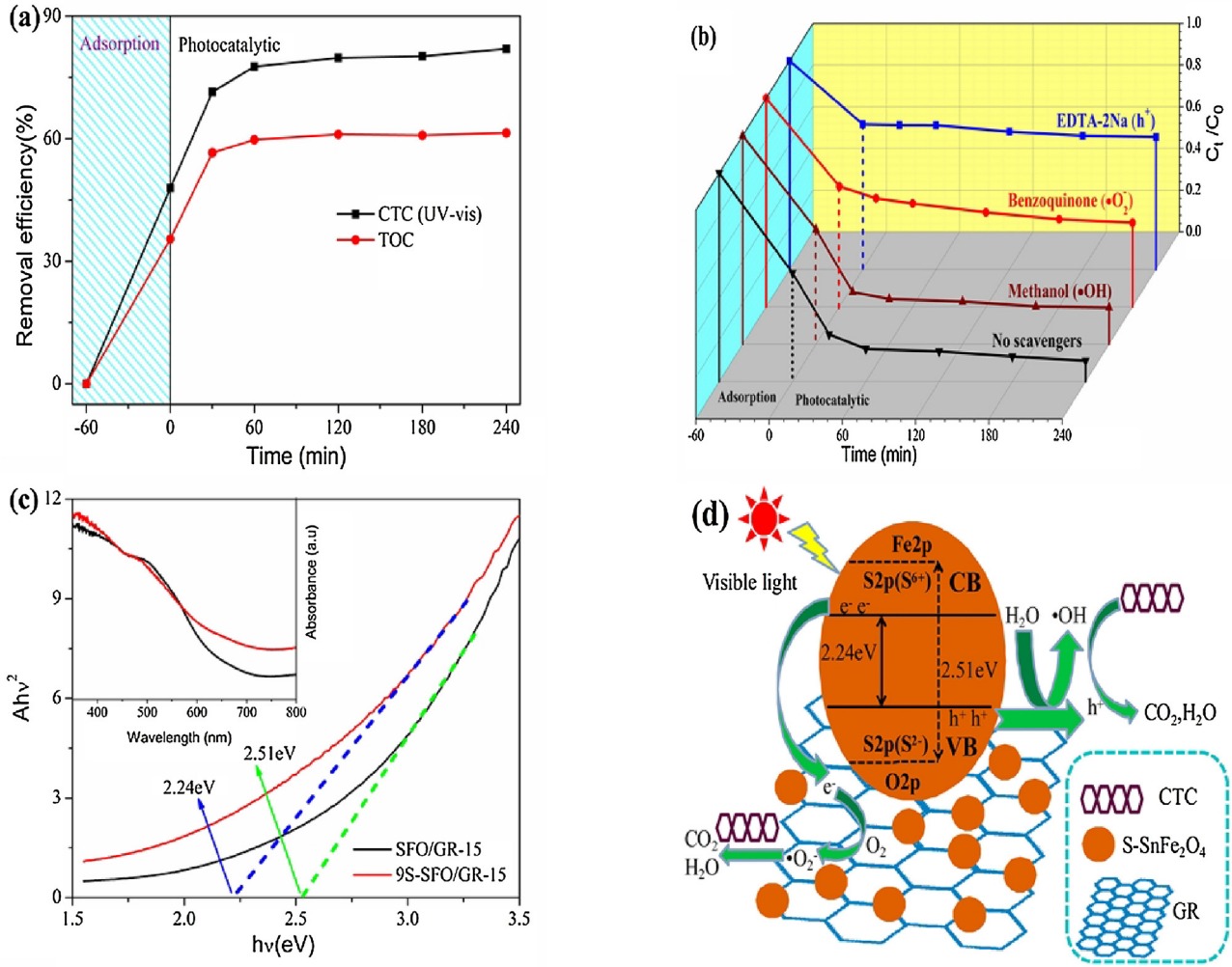

Fig. 7. (a) CTC and TOC removal efficiency in the presence of 9S-SFO/GR-15 after exposure to visible light; (b) effects of series of scavengers on the degradation efficiency of CTC; (c) UV–vis DRS of SFO/GR-15 and 9S-SFO/GR-15; (d) the mechanism illustration of high photocatalytic activity for S-SFO/GR.

3.4. The possible degradation mechanism

Fig. 7a compares the TOC measurement results with the absorption of CTC in the photocatalytic process. After 240 min irradiation, 39% of TOC still remained in the suspension, whereas only 18% CTC was detected from UV–vis absorption. The much slower reduction in TOC indicated that some intermediate organic species were still in the solution [59]. In our previous reports [5], the intermediate organic species during the photocatalytic process have been identified by liquid chromatography-mass spectrometry (LC–MS) at different retention times (RT) of CTC before and after the photocatalytic degradation (PD). Five main product ions at *m*/*z* 432.08 ($[M+H]^+$), 233.07 ($[M+H]^+$), 360.17 ($[M+H]^+$), 301.17 ($[M+H]^+$), and 199.01 ($[M+H]^+$), which correspond to the degradation products of $C_{21}H_{18}ClNO_7$, $C_{13}H_{12}O_4$, $C_{20}H_{25}NO_5$, $C_{19}H_{24}O_5$, and $C_9H_7ClO_3$, respectively, have been detected [4,5,54]. The chemical structural of those five PD products are described in Fig. S5. The PD products 1–4 may be further degraded by $^{\bullet}O_2^-$, •OH, and h^+ radicals to other chemicals with small molecular weights such as PD products 5. The PD products 5 were presumably further oxidized through ring-rupturing reactions, therefore H_2O and CO_2 could be obtained as the final degraded products with properly conditions.

To gain insight on the photocatalytic mechanism of 9S-SFO/GR-15 nanohybrids. Methanol (1:15/V:V), benzoquinone (10 mM) and EDTA-2Na (10 mM) were used as scavengers for the hydroxyl radical (•OH), the superoxide radical ($^{\bullet}O_2^-$) and the hole (h^+), respectively [14,31]. It can be seen from Fig. 7b that the degradation of CTC was decelerated after the addition of EDTA-2Na and methanol, indicating that h^+ and $^{\bullet}O_2^-$ are the main active species responsible for the oxidization of CTC under visible light irradiation. Moreover, the addition of benzoquinone has a negligible effect on CTC degradation. This shows that the •OH make a very small contribution to the photocatalytic reaction.

The UV–vis DRS of the SFO/GR-15 and 9S-SFO/GR-15 is shown in Fig. 7c. According to the spectra of Fig. 7c, 9S-SFO/GR-15 showed stronger absorption than SFO/GR-15 in visible light region, suggesting the materials should exhibit photocatalytic activity under visible light irradiation. The band gap energies of the as-prepared composites were calculated to be 2.51 eV (SFO/GR-15) and 2.24 eV (9S-SFO/GR-15) by Kubelka-Munk function [49]. The band gap of 9S-SFO/GR-15 was reduced remarkably as compared with SFO/GR-15. Since it has been reported that the introduction of GR has little effect on the band gap of $ZnFe_2O_4$ [44], the narrowed band gap of 9S-SFO/GR-15 can be mainly attributed to the S doping. The following reasons may explain the band gap narrowing effect. 1) Similar to the situation of S^{6+} takes the place of Ti^{4+}(0.64 Å) [42], the substitution of Fe^{3+}(0.65 Å) by S^{6+}(0.29 Å) might lead to the generation of localized S mid-gap levels located under the Fe2p conduction band(CB) in the SFO lattice. 2) S^{2-} (1.7 Å) can enter into the crystal lattice of SFO via replacing O^{2-} (1.22 Å) [60]. Since the

3p orbital energy of S is higher than O2p orbitals and located above the valence band (VB) of SFO, leading to the narrowed bandgap in S-SFO as compared to that of SFO (Fig. 7d).

Based on the above analysis, the photocatalytic reaction of CTC with the S-SFO/GR nanohybrids can be expressed as follows (Fig. 7d):

$$S\text{-}SnFe_2O_4/Graphene+CTC \xrightarrow{Adsorption} (S\text{-}SnFe_2O_4/Graphene)-CTC \quad (7)$$

$$S\text{-}SnFe_2O_4+h\nu \rightarrow S\text{-}SnFe_2O_4(e^-)+S\text{-}SnFe_2O_4(h^+) \quad (8)$$

$$S\text{-}SnFe_2O_4(e^-)+Graphene \rightarrow Graphene(e^-) \quad (9)$$

$$Graphene(e^-)+O_2 \rightarrow {}^{\bullet}O_2^- \quad (10)$$

$$S\text{-}SnFe_2O_4(h^+)+H_2O \rightarrow {}^{\bullet}OH+H^+ \quad (11)$$

$$CTC+{}^{\bullet}OH\ /h^+/{}^{\bullet}O_2^- \rightarrow \text{degraded products} \rightarrow H_2O+CO_2\uparrow \quad (12)$$

When the nanohybrids are exposed to an aqueous solution of CTC, the CTC molecules are partly adsorbed on the surface of S-SFO/GR due to the large surface area provided by GR and S-SFO nanoparticles (Eq. (7)). Since both S^{6+} and S^{2-} could introduce several new impurity levels in the energy bandgap of S-SFO, stronger absorption of visible light are expected in S-SFO/GR. Therefore more photogenerated e^- and h^+ should be accumulated in the CB and VB of S-SFO, respectively, due to visible light irradiation (Eq. (8)). The e^- can be transferred in two pathways in the S-SFO/GR nanohybrid. Firstly, because the CB of GR (−0.75 V vs. normal hydrogen electrode (NHE)) is more positive than that of SFO (−4.43 V vs. NHE) [12,44], the photogenerated e^- can be transferred readily from the CB of SFO to the surface of the GR nanosheets (Eq. (9)), and the photogenerated h^+ are left in the VB of S-SFO. Secondly, part of the photogenerated e^- could be captured by defects in S-SFO due to the substitution of S into the SFO lattice [41,61]. Therefore, the combination of S-SFO and GR results in a more effectively separation of the photogenerated e^--h^+ pairs.

We propose the following photolysis process. The migrated e^- are scavenged by O_2 in the solution, forming ${}^{\bullet}O_2{}^-$ radicals (Eq. (10)) [21], which are the main active species in the degradation of CTC. The h^+ left in the VB of S-SFO may oxidize CTC directly or will react with OH^- to generate reactive ${}^{\bullet}OH$ (Eq. (11)) [19], which was a strong oxidant for the mineralization of CTC. Moreover, Fe^{3+} was replaced by S^{6+} in S-SFO, and OH^- would be absorbed on the surface of S-SFO to keep a charge rebalance [42], and they could capture the photogenerated h^+ to form ${}^{\bullet}OH$. The ${}^{\bullet}O_2{}^-$, ${}^{\bullet}OH$, and h^+ radicals were the reactive species in S-SFO/GR visible light system, which can oxidize most of TCs antibiotics to H_2O, CO_2, and other mineral end-products (Eq. (12)) [49,62].

4. Conclusions

In summary, magnetically recoverable S-SFO/GR nanohybrids have been successfully developed via a solvothermal method and its photocatalytic activity was evaluated by CTC degradation process under visible light irradiation. Well dispersed S-SFO particles with sizes ranging from 20–30 nm were successfully attached on the GR nanosheets. As revealed by XPS analysis, S species doped into SFO are in S^{2-} and S^{6+} state. The photodegradation activities of 9S-SFO/GR-15 were demonstrated to be superior to those of the SFO, S-SFO, and SFO/GR. The significant enhancement in photoactivity can be attributed to the formation of the new impurity level and low e^--h^+ recombination rate. Furthermore, the 9S-SFO/GR-15 nanohybrids exhibited excellent reusability, which was evidenced by their consistent photocatalytic performance and the absence of any observable changes in structural and chemical properties, even after five cycles of operation during the photocatalytic reaction. The catalyst can be easily separated from the catalytic solution using a lab magnet. In view of the high activity and recyclable magnetic separation of 9S-SFO/GR-15 nanohybrids, it has potential applications in the oxidation of organic pollutants in wastewater.

Acknowledgments

This research was supported by the Basic Science Research Program through the National Research Foundation of Korea funded by the Ministry of Science, ICT and Future Planning (2014R1A1A3049826 and 2014R1A2A1A11051245). WL thanks to the Priority Research Centers Program (2009-0093823) through the National Research Foundation of Korea (NRF). SEM characterization in this research was supported by Nano-material Technology Development Program through the National Research Foundation of Korea (NRF) funded by the Ministry of Science, ICT and Future Planning (2009-0082580). The XPS measurement was performed in Busan Center of Korea Basic Science Institute (KBSI).

Appendix A. Supplementary data

Supplementary data associated with this article can be found, in the online version, at http://dx.doi.org/10.1016/j.jhazmat.2017.05.057.

References

[1] C. Zhao, Y. Zhou, D.J. de Ridder, J. Zhai, Y. Wei, H. Deng, Advantages of TiO_2/5A composite catalyst for photocatalytic degradation of antibiotic oxytetracycline in aqueous solution: comparison between TiO_2 and TiO_2/5A composite system, Chem. Eng. J. 248 (2014) 280–289.
[2] J.J. Salazar-Rábago, M. Sánchez-Polo, J. Rivera-Utrilla, R. Leyva-Ramos, R. Ocampo- Pérez, Role of $^-[O_2]^*$ in chlortetracycline degradation by solar radiation assisted by ruthenium metal complexes, Chem. Eng. J. 284 (2016) 896–904.
[3] R. Daghrir, P. Drogui, N. Delegan, M.A. El Khakani, Electrochemical degradation of chlortetracycline using N-doped Ti/TiO_2 photoanode under sunlight irradiations, Water Res. 47 (2013) 6801–6810.
[4] D. Bu, H. Zhuang, Biotemplated synthesis of high specific surface area copper-doped hollow spherical titania and its photocatalytic research for degradating chlorotetracycline, Appl. Surf. Sci. 265 (2013) 677–685.
[5] Y. Jia, J. Liu, S. Cha, S. Choi, Y.C. Park, C. Liu, Magnetically separable Au-TiO_2/nanocube $ZnFe_2O_4$ composite for chlortetracycline removal in wastewater under visible light, J. Ind. Eng. Chem. 47 (2017) 303–314.
[6] L. Jing, W. Zhou, G. Tian, H. Fu, Surface tuning for oxide-based nanomaterials as efficient photocatalysts, Chem. Soc. Rev. 42 (2013) 9509–9549.
[7] H.H. Chen, E.N. Charith, H.G. Vicki, Titanium dioxide photocatalysis in atmospheric chemistry, Chem. Rev. 112 (2012) 5919–5948.
[8] M. Pelaez, A. Armah, E. Stathatos, P. Falaras, D.D. Dionysiou, Visible light-activated N-F-codoped TiO_2 nanoparticles for the photocatalytic degradation of microcystin-LR in water, Catal. Today 144 (2009) 19–25.
[9] Z. Zhu, F. Liu, H. Zhang, J. Zhang, L. Han, Photocatalytic degradation of 4-chlorophenol over Ag/MFe_2O_4 (M = Co, Zn, Cu, and Ni) prepared by a modified chemical co-precipitation method: a comparative study, RSC Adv. 5 (2015) 55499–55512.
[10] C. Cai, Z. Zhang, J. Liu, N. Shan, H. Zhang, D.D. Dionysiou, Visible light-assisted heterogeneous Fenton with $ZnFe_2O_4$ for the degradation of Orange II in water, Appl. Catal. B 182 (2016) 456–468.
[11] X. Zhao, X. Liu, A novel magnetic $NiFe_2O_4$@ graphene–Pd multifunctional nanocomposite for practical catalytic application, RSC Adv. 5 (2015) 79548–79555.
[12] K.T. Lee, S.Y. Lu, A cost-effective stable, magnetically recyclable photocatalyst of ultra-high organic pollutant degradation efficiency: $SnFe_2O_4$ nanocrystals from a carrier solvent assisted interfacial reaction process, J. Mater. Chem. A 3 (2015) 12259–12267.
[13] S. Huang, Y. Xu, M. Xie, H. Xu, M. He, J. Xia, H. Li, Synthesis of magnetic $CoFe_2O_4$/g-C_3N_4 composite and its enhancement of photocatalytic ability under visible-light, Colloids Surf. A 478 (2015) 71–80.
[14] Z. Tong, D. Yang, J. Shi, Y. Nan, Y. Sun, Z. Jiang, Three-dimensional porous aerogel constructed by g-C_3N_4 and graphene oxide nanosheets with excellent visible-light photocatalytic performance, ACS Appl. Mater. Interfaces 7 (2015) 25693–25701.
[15] S. Han, L. Hu, Z. Liang, S. Wageh, A.A. Al-Ghamdi, Y. Chen, X. Fang, One-step hydrothermal synthesis of 2D hexagonal nanoplates of α-Fe_2O_3/graphene composites with enhanced photocatalytic activity, Adv. Funct. Mater. 24 (2014) 5719–5727.
[16] M.M. Mohamed, I. Ibrahim, T.M. Salama, Rational design of manganese ferrite-graphene hybrid photocatalysts: efficient water splitting and effective elimination of organic pollutants, Appl. Catal. A 524 (2016) 182–191.

[17] X. Song, Q. Shi, H. Wang, S. Liu, C. Tai, Z. Bian, Preparation of Pd-Fe/graphene catalysts by photocatalytic reduction with enhanced electrochemical oxidation-reduction properties for chlorophenols, Appl. Catal. B 203 (2017) 442–451.
[18] L. Gan, S. Shang, C.W.M. Yuen, S.X. Jiang, E. Hu, Hydrothermal synthesis of magnetic $CoFe_2O_4$/graphene nanocomposites with improved photocatalytic activity, Appl. Surf. Sci. 351 (2015) 140–147.
[19] D. Yang, J. Feng, L. Jiang, X. Wu, L. Sheng, Y. Jiang, Z. Fan, Photocatalyst interface engineering: spatially confined growth of $ZnFe_2O_4$ within graphene networks as excellent visible-light-driven photocatalysts, Adv. Funct. Mater. 25 (2015) 7080–7087.
[20] S.Q. Liu, B. Xiao, L.R. Feng, S.S. Zhou, Z.G. Chen, C.B. Liu, Z.D. Meng, Graphene oxide enhances the Fenton-like photocatalytic activity of nickel ferrite for degradation of dyes under visible light irradiation, Carbon 64 (2013) 197–206.
[21] D. Zhang, Q. Wang, L. Wang, L. Zhang, Magnetically separable $CdFe_2O_4$/graphene catalyst and its enhanced photocatalytic properties, J. Mater. Chem. A 3 (2015) 3576–3585.
[22] I. Shakir, M. Sarfraz, Z. Ali, M.F. Aboud, P.O. Agboola, Magnetically separable and recyclable graphene-$MgFe_2O_4$ nanocomposites for enhanced photocatalytic applications, J. Alloys Compd. 660 (2016) 450–455.
[23] P. Chen, X. Xing, H. Xie, Q. Sheng, H. Qu, High catalytic activity of magnetic $CuFe_2O_4$/graphene oxide composite for the degradation of organic dyes under visible light irradiation, Chem. Phys. Lett. 660 (2016) 176–181.
[24] S. Bai, X. Shen, X. Zhong, Y. Liu, G. Zhu, X. Xu, K. Chen, One-pot solvothermal preparation of magnetic reduced graphene oxide-ferrite hybrids for organic dye removal, Carbon 50 (2012) 2337–2346.
[25] L. Liu, G. Zhang, L. Wang, T. Huang, L. Qin, Highly active S-modified $ZnFe_2O_4$ heterogeneous catalyst and its photo-Fenton behavior under UV-visible irradiation, Ind. Eng. Chem. Res. 50 (2011) 7219–7227.
[26] X. Guo, H. Li, S. Zhao, Fast degradation of Acid Orange II by bicarbonate-activated hydrogen peroxide with a magnetic S-modified $CoFe_2O_4$ catalyst, J. Taiwan Inst. Chem. Eng. 55 (2015) 90–100.
[27] D. Cao, X. Wang, L. Pan, H. Li, P. Jing, J. Wang, Q. Liu, Nonmetal sulfur-doped coral-like cobalt ferrite nanoparticles with enhanced magnetic properties, J. Mater. Chem. C 4 (2016) 951–957.
[28] L. Wang, W. Jia, X. Liu, J. Li, M.M. Titirici, Sulphur-doped ordered mesoporous carbon with enhanced electrocatalytic activity for the oxygen reduction reaction, J. Energy Chem. 25 (2016) 566–570.
[29] S.D. Senol, O. Ozturk, C. Terzioğlu, Effect of boron doping on the structural, optical and electrical properties of ZnO nanoparticles produced by the hydrothermal method, Ceram. Int. 41 (2015) 11194–11201.
[30] X. Wang, H. Jiang, Y. Liu, M. Gao, Rapid microwave-assisted hydrothermal synthesis of Sm, N, and P tridoped anatase-TiO_2 nanosheets from $TiCl_4$ hydrolysis, Mater. Lett. 147 (2015) 72–74.
[31] Y. Jia, D.H. Kim, B.W. Lee, S.J. Rhee, S. Kang, T. Lee, C. Liu, One-pot solvothermal synthesis of magnetic $SnFe_2O_4$ nanoparticles and their performance in the photocatalytic degradation of chlortetracycline with visible light radiation, RSC Adv. 6 (2016) 76542–76550.
[32] Y. Jia, S.J. Rhee, C. Liu, Synthesis of magnetic recoverable g-C_3N_4/$SnFe_2O_4$ composite with enhanced visible light photocatalytic property, Mater. Lett. 188 (2017) 338–342.
[33] Y. Wu, Z. Li, J. Chen, C. Yu, X. Huang, C. Zhao, W. Lü, Graphene nanosheets decorated with tunable magnetic nanoparticles and their efficiency of wastewater treatment, Mater. Res. Bull. 68 (2015) 234–239.
[34] K. Bindu, K. Sridharan, K.M. Ajith, H.N. Lim, H.S. Nagaraja, Microwave assisted growth of stannous ferrite microcubes as electrodes for potentiometric nonenzymatic H_2O_2 sensor and supercapacitor applications, Electrochim. Acta 217 (2016) 139–149.
[35] Y. Shi, K. Zhou, B. Wang, S. Jiang, X. Qian, Z. Gui, Y. Hu, Ternary graphene–$CoFe_2O_4$/CdS nanohybrids: preparation and application as recyclable photocatalysts, J. Mater. Chem. A 2 (2014) 535–544.
[36] T. Soltani, B.K. Lee, Sono-synthesis of nanocrystallized $BiFeO_3$/reduced graphene oxide composites for visible photocatalytic degradation improvement of bisphenol A, Chem. Eng. J. 306 (2016) 204–213.
[37] J.C. Yu, W. Ho, J. Yu, H. Yip, P.K. Wong, J. Zhao, Efficient visible-light-induced photocatalytic disinfection on sulfur-doped nanocrystalline titania, Environ. Sci. Technol. 39 (2005) 1175–1179.
[38] X. Yang, F. Qian, Y. Wang, M. Li, J. Lu, Y. Li, M. Bao, Constructing a novel ternary composite $(C_{16}H_{33}(CH_3)_3N)_4W_{10}O_{32}$/g-$C_3N_4$/rGO with enhanced visible-light-driven photocatalytic activity for degradation of dyes and phenol, Appl. Catal. B 200 (2017) 283–296.
[39] S.F. Mansour, O.M. Hemeda, S.I. El-Dek, B.I. Salem, Influence of La doping and synthesis method on the properties of $CoFe_2O_4$ nanocrystals, J. Magn. Magn. Mater. 420 (2016) 7–18.
[40] J. Liu, H. Bai, Y. Wang, Z. Liu, X. Zhang, D.D. Sun, Self-assembling TiO_2 nanorods on large graphene oxide sheets at a two-phase interface and their anti-recombination in photocatalytic applications, Adv. Funct. Mater. 20 (2010) 4175–4181.
[41] S. Bian, C. Shen, Y. Qian, J. Liu, F. Xi, X. Dong, Facile synthesis of sulfur-doped graphene quantum dots as fluorescent sensing probes for Ag^+ ions detection, Sens. Actuators B 242 (2017) 231–237.
[42] D. Ma, Y. Xin, M. Gao, J. Wu, Fabrication and photocatalytic properties of cationic and anionic S-doped TiO_2 nanofibers by electrospinning, Appl. Catal. B 147 (2014) 49–57.
[43] G.H. Zhang, P.Y. Wang, X.Y. Deng, Y. Chen, D.J. Gengzang, X.L. Wang, W.J. Chen, CTAB-assisted synthesis of 3D Sn doped ZnO nanostructures with enhanced acetone sensing performance, Mater. Lett. 162 (2016) 265–268.
[44] A.H. Mady, M.L. Baynosa, D. Tuma, J.J. Shim, Facile microwave-assisted green synthesis of Ag-$ZnFe_2O_4$@ rGO nanocomposites for efficient removal of organic dyes under UV-and visible-light irradiation, Appl. Catal. B 203 (2017) 416–427.
[45] T. Soltani, B.K. Lee, Novel and facile synthesis of Ba-doped $BiFeO_3$ nanoparticles and enhancement of their magnetic and photocatalytic activities for complete degradation of benzene in aqueous solution, J. Hazard. Mater. 316 (2016) 122–133.
[46] S. Wang, J. Zhang, J. Yang, X. Gao, H. Zhang, Y. Wang, Z. Zhu, Spinel $ZnFe_2O_4$ nanoparticle-decorated rod-like ZnO nanoheterostructures for enhanced gas sensing performances, RSC Adv. 5 (2015) 10048–10057.
[47] L. Xu, J. Wang, Magnetic nanoscaled Fe_3O_4/CeO_2 composite as an efficient Fenton-like heterogeneous catalyst for degradation of 4-chlorophenol, Environ. Sci. Technol. 46 (2012) 10145–10153.
[48] T. Wang, G. Xiao, C. Li, S. Zhong, F. Zhang, One-step synthesis of a sulfur doped Bi_2WO_6/Bi_2O_3 composite with enhanced visible-light photocatalytic activity, Mater. Lett. 138 (2015) 81–84.
[49] A. Kumar, T. Mohanty, Electro-optic modulation induced enhancement in photocatalytic activity of N-doped TiO_2 thin films, J. Phys. Chem. C 118 (2014) 7130–7138.
[50] Y. Li, Z. Zhang, L. Pei, X. Li, T. Fan, J. Ji, M. Ye, Multifunctional photocatalytic performances of recyclable Pd-$NiFe_2O_4$/reduced graphene oxide nanocomposites via different co-catalyst strategy, Appl. Catal. B 190 (2016) (2016) 1–11.
[51] Y. Yao, J. Qin, H. Chen, F. Wei, X. Liu, J. Wang, S. Wang, One-pot approach for synthesis of N-doped TiO_2/$ZnFe_2O_4$ hybrid as an efficient photocatalyst for degradation of aqueous organic pollutants, J. Hazard. Mater. 291 (2015) 28–37.
[52] M.W. Lam, K. Tantuco, S.A. Mabury, PhotoFate: a new approach in accounting for the contribution of indirect photolysis of pesticides and pharmaceuticals in surface waters, Environ. Sci. Technol. 37 (2003) 899–907.
[53] J. Hirayama, Y. Kamiya, Combining the photocatalyst Pt/TiO_2 and the nonphotocatalyst SnPd/Al_2O_3 for effective photocatalytic purification of groundwater polluted with nitrate, ACS Catal. 4 (2014) 2207–2215.
[54] W.R. Chen, C.H. Huang, Transformation kinetics and pathways of tetracycline antibiotics with manganese oxide, Environ. Pollut. 159 (2011) 1092–1100.
[55] L. Shi, K. Chen, R. Du, A. Bachmatiuk, M.H. Rümmeli, K. Xie, Z. Liu, Scalable seashell-based chemical vapor deposition growth of three-dimensional graphene foams for oil–water separation, J. Am. Chem. Soc. 138 (2016) 6360–6363.
[56] R. Daghrir, P. Drogui, N. Delegan, M.A. El Khakani, Removal of chlortetracycline from spiked municipal wastewater using a photoelectrocatalytic process operated under sunlight irradiations, Sci. Total Environ. 466 (2014) 300–305.
[57] E. Bizani, K. Fytianos, I. Poulios, V. Tsiridis, Photocatalytic decolorization and degradation of dye solutions and wastewaters in the presence of titanium dioxide, J. Hazard. Mater. 136 (2006) 85–94.
[58] H. Lu, E.E. Salabas, F. Schüth, Magnetic nanoparticles: synthesis, protection, functionalization, and application, Angew. Chem. Int. Ed. 46 (2007) 1222–1244.
[59] Y. Hu, K. Zhou, B.Y. Chen, C.T. Chang, Graphene/TiO_2/ZSM-5 composites synthesized by mixture design were used for photocatalytic degradation of oxytetracycline under visible light: mechanism and biotoxicity, Appl. Surf. Sci. 362 (2016) 329–334.
[60] F.F. Li, D.R. Liu, G.M. Gao, B. Xue, Y.S. Jiang, Improved visible-light photocatalytic activity of $NaTaO_3$ with perovskite-like structure via sulfur anion doping, Appl. Catal. B 166 (2015) 104–111.
[61] S.H. Nam, T.K. Kim, J.H. Boo, Physical property and photo-catalytic activity of sulfur doped TiO_2 catalysts responding to visible light, Catal. Today 185 (2012) 259–262.
[62] F. Chen, Q. Yang, J. Sun, F. Yao, S. Wang, Y. Wang, G. Zeng, Enhanced photocatalytic degradation of tetracycline by AgI/$BiVO_4$ heterojunction under visible-Light irradiation: mineralization efficiency and mechanism, ACS Appl. Mater. Interfaces 8 (2016) 32887–32900.